FINITE ELEMENT ANALYSIS OF IN-PLANE CYCLIC LOADING ON MASONRY WALLS WITH TRADITIONAL MORTARS USED IN NEPAL USING SIMPLIFIED MICRO-MODELING

Ratna Shova Prajapati[1], **Rameswor Shrestha**[1,2]*, **Anil Kasula**[1]

[1] Department of Civil Engineering, Khwopa College of Engineering, Bhaktapur, Nepal
[2] Department of Disaster Mitigation for Structures, Tongji University, Shanghai, China

---

Abstract

Masonry construction relies critically on the mechanical performance of mortar joints, especially under cyclic loading such as seismic action. This study numerically investigates the in-plane cyclic behavior of masonry walls built with cement, lime-surkhi, and mud mortars using a validated simplified micro-modeling approach in ABAQUS. The finite element model demonstrates strong agreement with experimental benchmarks, replicating load-displacement response, crack propagation, and stress redistribution with a root mean square error of 1.3%. Under cyclic loading, each mortar type exhibited distinct degradation patterns quantified by key metrics: cement mortar showed high initial stiffness (170 kN/mm) but rapid stiffness loss of approximately 75% within the first 1 mm displacement, indicating swift yielding despite good energy dissipation. Lime-surkhi mortar exhibited moderate ductility with a gradual stiffness reduction from 25 kN/mm to 5 kN/mm over 4 mm displacement. Mud mortar demonstrated negligible structural capacity, with brittle failure occurring at 15 kN and 3 mm displacement, constant low stiffness (5 kN/mm), and minimal energy dissipation. Analysis of equivalent plastic strain (PEEQT) and tensile damage (DAMAGET) provided further insight into mortar-specific damage evolution. These quantitative findings offer a clear performance hierarchy to inform the resilient design and restoration of masonry structures, particularly those of cultural and historical significance.

Keywords: Masonry wall, Cement mortar, Lime-surkhi mortar, Mud mortar, Simplified micro-modeling, Cyclic loading

---

1. Introduction

Masonry, one of the oldest and most fundamental building techniques, involves the systematic arrangement of stone, bricks, or other modular units, bound together with or without mortar. Renowned for its durability, low maintenance, versatility, aesthetic appeal, and structural solidity, masonry remains widely employed in construction. From an engineering perspective, masonry structures primarily resist compressive stresses. However, their strength is governed by the composite interaction between the units (e.g., bricks or stones) and the mortar. The mortar, being the weakest component in the system, critically influences the overall mechanical performance of masonry under load (Liang et al., 2023). Variations in mortar composition and properties such as strength, adhesion, and elasticity directly affect the structural integrity and failure mechanisms of masonry assemblies (Singh and Munjal, 2017). Consequently, investigating the effects of different mortar types is essential to comprehensively understand and optimize the mechanical behavior of masonry systems. Engineering norms and codes (“Building Code Requirements and Specification for Masonry Structures”, 2013; “Design of Masonry Structures - Part 1-1”, 2005; “Code for Design of Masonry Structures”, 2011) specify key mechanical properties of masonry, including compressive strength, elastic modulus, Poisson’s ratio, stress-strain relationships, and other macroscopic parameters. These

*Corresponding author: Rameswor Shrestha
Department of Disaster Mitigation for Structures,
Tongji University, Shanghai, China
Department of Civil Engineering, Khwopa College of Engineering, Bhaktapur, Nepal
Email: rameswor.sth@khwopa.edu.np
(Received: August 31, 2025, Accepted: January 14, 2026)
https://doi.org/10.3126/jsce.v13i2.96571

international standards emphasize a critical observation: the strength of masonry is significantly lower than that of its constituent units and mortar. Furthermore, studies have demonstrated that Young's modulus and masonry strength exhibit negligible dependence on the structural scale of masonry assemblies (Knox et al., 2018). Mechanical properties of masonry are typically determined through axial compression tests (Jafari et al., 2017). Researchers have conducted extensive experimental studies to correlate these properties with factors such as mortar grade (Liang et al., 2023), water-cement ratio (Minafò and La Mendola, 2018), and damage evolution mechanisms in masonry under load (Ravula and Subramaniam, 2017). However, inherent variability arises due to the unique characteristics of individual units, mortar type, batch composition, mortar joint thickness, and unit arrangement. These factors collectively introduce uncertainty into the homogenized assessment of masonry behavior. The evolution of masonry structures has historically depended on regional material availability and technological advancements. While masonry units have remained largely unchanged over time, mortar formulations have evolved alongside innovations in construction techniques and the accessibility of binding agents. For instance, the Romans pioneered the use of volcanic ash in mortar to enhance resistance against water penetration and freeze-thaw cycles (Degryse et al., 2002). Similarly, traditional Chinese mortars incorporated lime-based blends mixed with organic additives such as egg white, sticky rice, animal hair, molasses, and even blood, tailored to varying proportions for specific structural needs (Fang et al., 2014). In Nepal, lime is mixed with brick dust (Surkhi) to create a mortar called Bajra mortar (Bahadur et al., 2021; Bijukchhen et al., 2017). This Bajra mortar is specially used in monuments as a binding material for brick and stone masonry. Such regional variations in mortar composition dictated by material availability, cultural practices, and environmental demands underscore the intricate relationship between localized resources and masonry innovation. Masonry exhibits pronounced anisotropic behavior due to its heterogeneous composition of distinct materials, masonry units and mortar joints. Experimental studies reveal that even structurally identical masonry walls often yield non-identical results (Alcaino and Santa-Maria, 2008). The difference in result is cause due to variation in workmanship, non-identical masonry unit property, and accurate detection and monitoring of cracks. In contrast, numerical modeling offers a reliable and consistent alternative to experimental approaches (Zhang et al., 2017), enabling systematic investigation of masonry mechanics. Diverse numerical frameworks, such as the finite element method (FEM), discrete element method (DEM), and applied element method (AEM) (Khattak et al., 2023), have been utilized to simulate both linear elastic behavior and nonlinear mechanisms like crack propagation and structural collapse under varying loading conditions. Among these, the finite element method (FEM) is used in this paper for the numerical analysis. FEM for masonry can be classified into three categories (Abdulla et al., 2017; Senthivel and Lourenço, 2009): micro-modelling, simplified micro-modelling and macro-modelling. The detailed micro-modelling shown in Figure 1a explicitly represents both units and mortar joints with continues and discontinues interface elements, providing highly accurate results but requiring significant computational effort. The simplified micro-modelling (SM) approach as shown in Figure 1b reduces complexity by expanding the units to include mortar thickness and then using discontinuous elements only at the interfaces (Lourenço and Rots, 1997). Finally, the macro-modelling method shown in Figure 1c treats masonry as a homogeneous material with smeared properties, offering lower computational demand while sacrificing the fine-detail accuracy seen in micro-modelling (Lourenco, 1996).

The simplified micro-modeling (SM) approach was employed to investigate masonry behavior and analyze the interaction between masonry units and mortar joints. This methodology also successfully captures deformation patterns, failure mechanisms, stress distribution, and crack propagation while maintaining lower computational complexity (Xia et al., 2023). Further extended the SM framework to a three-dimensional (3D) model, validating it against experimental cyclic quasi-static tests. Their simulations demonstrated strong agreement with experimental results, particularly in predicting crack formation and masonry crushing (Tariq et al., 2023). In this study, a 3D simplified micro-modeling approach is developed to simulate the in-plane behavior of masonry structures. The concrete damage plasticity (CDP) model is applied to the masonry unit continuum to simulate crushing behavior, while cohesive interfaces governed by a traction-separation law are utilized to model crack initiation and propagation at mortar interface. The numerical model is implemented using the finite element (FE) software ABAQUS, with quasi-static monotonic and cyclic loading applied to the masonry wall. The aim of this study is to quantify stiffness degradation, displacement, and tensile damage to the walls due to cyclic loads to better understand the suitability and performance of contemporary and traditional mortars namely; cement, lime-surkhi, and mud mortar used in masonry subjected to cyclic loading conditions. The framework not only replicates the detailed mechanical response of the masonry wall but also accurately predicts crack patterns and their evolution under load.

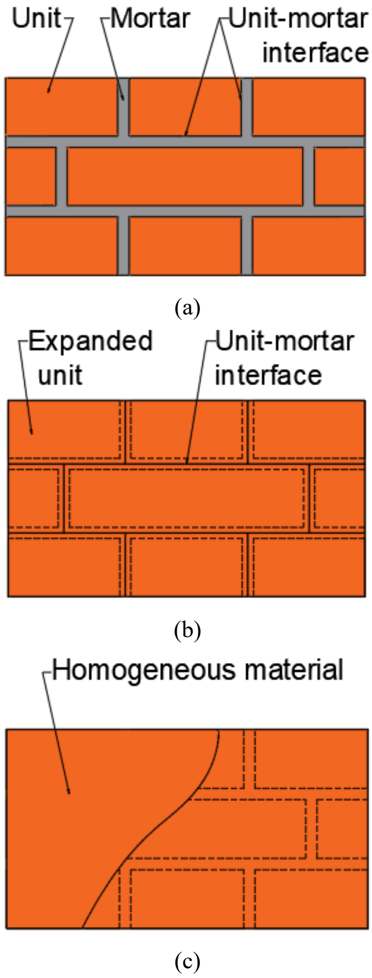

Figure 1: Finite element modelling approach of brick masonry: (a) detailed micro-model with interface, (b) simplified micro-model, (c) solid macro-model (Abdulla et al., 2017)

2. Modelling Approach

The constitutive model for the simplified micromodel of masonry characterizes the unit as a solid continuum and the joint as a zero-thickness interface. Additionally, it explicitly defines distinct failure modes for both the unit and the joint interface, enabling precise simulation of their mechanical responses under load.

2.1. Modelling of Masonry Unit

The constitutive behavior of masonry units is modeled using the concrete damage plasticity (CDP) framework. This approach characterizes the material as an isotropic continuum, where elastic stiffness gradually degrades under the development of inelastic strain. The CDP model captures the nonlinear response of masonry under both compressive crushing and tensile fracture, simulating progressive damage accumulation. Compressive and tensile stress-strain relationships for the material are governed by Equations (1) and (2), respectively, which define the hardening/softening behavior of the CDP model (Zhang et al., 2017).

$$\sigma/f_{cu} = \frac{h}{1+(h-1)(\varepsilon/\varepsilon_{cu})^{h/(h-1)}}\varepsilon/\varepsilon_{cu} \tag{1}$$

$$\sigma/f_{tu} = \begin{cases} \varepsilon/\varepsilon_{tu}, & \varepsilon/\varepsilon_{tu} \le 1 \\ (\varepsilon/\varepsilon_{tu})/(2(\varepsilon/\varepsilon_{tu}-1)^{1.7}+\varepsilon/\varepsilon_{tu}), & \varepsilon/\varepsilon_{tu} > 1 \end{cases} \tag{2}$$

where, f_{cu} and f_{tu} represent the peak compressive and tensile strength of unit, ε_{cu} and ε_{tu} are peak strain at compression and tension respectively. The compressive factor, h, is set to 1.633, as suggested by (Zhang et al. (2017)).

Under compressive or tensile loading, the stiffness of masonry unit degrades non-linearly. This degradation is quantified through a dimensionless scalar variable d as defined in Equation (3) ("Code for Design of Concrete Structures", 2010;Zhang et al., 2017). The damage variable is formulated as a function of the applied stress (σ), the corresponding strain (ε) and the inelastic elastic modulus (E_0), capturing the progressive loss of material integrity due to inelastic deformation.

$$d = 1 - \sqrt{\sigma/(E_0\varepsilon)} \tag{3}$$

2.2. Joint Interface Elastic Response

The joint element interface accommodates displacement discontinuities during initial loading stages, characterized by a linear traction-displacement constitutive relationship. This linear elastic behavior is formulated through a stiffness matrix, where the nominal traction vector ($\mathbf{t}$) is related to the elastic stiffness ($\mathbf{K}$) and the separation vector ($\boldsymbol{\delta}$) of the joint interface, as defined in Equation (4) (Abdulla et al., 2017;Lourenço and Rots, 1997).

$$\mathbf{t} = \begin{bmatrix} t_n \\ t_s \\ t_t \end{bmatrix} = \begin{bmatrix} K_n & 0 & 0 \\ 0 & K_s & 0 \\ 0 & 0 & K_t \end{bmatrix} \begin{bmatrix} \delta_n \\ \delta_s \\ \delta_t \end{bmatrix} = \mathbf{K}\boldsymbol{\delta} \tag{4}$$

The components of stiffness matrix (K) in Equation (4) must accurately replicate the mechanical behavior of the real brick mortar joints under representative boundary conditions. The matrix components are determined from the elastic properties of the individual masonry constituents and geometric parameters, particularly the joint thickness, to ensure consistency with the original composite behavior. The normal stiffness component K_n depends on the elastic modulus of both masonry unit (E_u) and mortar (E_m), along with the mortar thickness (h_m) as expressed in Equation (5). Similarly, the shear stiffness component K_s and K_t both along and perpendicular to the shear plane are determined by the shear moduli of the masonry unit (G_u) and mortar (G_m) as given in Equation (6).

$$K_n = \frac{E_u E_m}{h_m(E_u - E_m)} \tag{5}$$

$$K_s = K_t = \frac{G_u G_m}{h_m(G_u - G_m)} \tag{6}$$

2.3. Joint Interface Plastic Response

The plastic response of the joint represents crack initiation and propagation, accompanied by progressive degradation of the mortar joint stiffness. Damage evolution is driven by the friction coefficient and fracture energy of the interface material. Mixed-mode failure is characterized by a quadratic stress criterion that combines normal tensile stress and shear stresses in two orthogonal directions, as defined in Equation (7). This criterion ensures a unified representation of interface failure under complex failure mode.

$$\frac{\langle t_n \rangle}{t_n^{\max}}^2 + \frac{t_s}{t_s^{\max}}^2 + \frac{t_t}{t_t^{\max}}^2 = 1 \tag{7}$$

The Macaulay bracket operator in Equation (7) ensures the exclusion of compressive stress contributions to the fracture behavior of the interface in the normal direction. Concurrently, the shear strength of the mortar joint is determined via the Mohr-Coulomb failure criterion, shown in Equation (8), which incorporates governing factors such as cohesion, friction coefficient, and normal compressive stress to model shear resistance under compressive loading.

$$\tau_{\text{crit}} = c + \mu\sigma_n \tag{8}$$

Furthermore, the critical mixed-mode fracture energy (G_{TC}) as defined in Equation (9) is determined using the Benzeggagh-Kenane (BK) criterion, which is particularly suited for scenarios where the critical fracture energies in normal tensile (Mode I) and shear modes (Mode II and Mode III) are equivalent to a condition inherent to masonry joints. Within the BK formulation, the exponent η is assigned a value of 2 to reflect the brittle fracture behavior typical of masonry interfaces, aligning with experimental observations of rapid crack propagation and minimal plastic deformation (Abdulla et al., 2017;Benzeggagh and Kenane, 1996).

$$G_{TC} = G_{IC} + (G_{IIC} - G_{IC}) \left(\frac{G_{IIC}}{G_{IC} + G_{IIC}} \right)^{\eta} \tag{9}$$

The normal tensile and shear fracture energy are calculated using formulations defined in Equations (10) to (12), which integrate experimental and analytical frameworks to quantify energy dissipation during crack initiation and propagation (Lotif and Shing, 1994;Yuen et al., 2019). These relationships account for distinct failure mechanisms in quasi-brittle materials such as masonry, emphasizing brittle fracture and rapid damage evolution under load.

$$G_{\min} = \frac{f_t^2}{2K_n} \tag{10}$$

$$G_{IC} = 5G_{\min} \tag{11}$$

$$G_{IIC} = 6.94G_{IC} \tag{12}$$

3. Finite Element Modelling and Validation

3.1. Framework for Element Modelling

The 3D ABAQUS/standard simplified micro-model defines the linear and nonlinear behavior of unit and interface. The expanded masonry units are discretized using 3D hexahedral eight-nodded linear brick elements with reduced integration (C3D8R) and incorporating hourglass stabilization to mitigate non-physical deformation modes while maintaining computational efficiency in nonlinear simulations. The joint interfaces are modeled using a surface-based cohesive behavior governed by a traction-separation constitutive law applied to both bed and head joints. This framework integrates a linear elastic phase to define the undamaged interface response, followed by damage initiation triggered by mixed-mode failure criteria and subsequent damage evolution characterized by fracture energy dissipation with exponent of 2. In the case for stabilization, the viscosity coefficient parameter of 0.002 was adopted (Abdulla et al., 2017).For tangential interactions, Coulomb friction with a defined coefficient governs shear behavior, while normal interactions adhere to a hard-contact pressure-overclosure relationship, permitting compressive force transmission upon contact and separation under tension. Adjacent masonry units are connected via a surface-to-surface contact discretization method incorporating a finite sliding formulation, which accurately resolves contact pressures and frictional forces during large relative displacements. The hard-contact assumption enforces geometric compatibility between units, preventing penetration while ensuring realistic load transfer under compression. In the case for mesh size, constant mesh size of 7×2×3 is adapted for full brick, while 4×3×2 mesh size is used for half brick (Abdulla et al., 2017) as shown in Figure 2a.

3.2. Model Validation Under In-plane Loading

The numerical model is validated against experimental data from unreinforced masonry shear walls tested by Raijmakers and Vermeltfoort (1992) and later documented by Lourenco (1996). The specimen, a 100 mm thick masonry shear wall with approximate width and height dimensions of 990 mm × 1106 mm respectively, comprises 18 courses of solid clay bricks (full brick: 210 mm × 52 mm × 100 mm; half-brick: 115 mm × 52 mm× 100 mm). A 10 mm thick mortar joints with volumetric mix ratio 1:2:9 cement:lime:sand is used. Both top and bottom courses are restrained via steel beams, with the bottom beam fully fixed. A vertical compressive stress of 0.3 MPa is applied to the top beam, after which vertical displacement is constrained, and a monotonic horizontal load is applied under displacement control using the ABAQUS implicit solver, Figure 2b.

The simulation replicates the experimental boundary conditions and loading protocol to assess the in-plane shear behavior of the masonry structure. Key validation metrics includes load-displacement response, crack propagation patterns, and stress distribution which are rigorously compared against experimental benchmarks. The constitutive behavior of the brick units is governed by the elastoplastic formulations defined in Equations (1) to (3), while the CDP model incorporates a yield surface derived from the failure criteria proposed in Lee and Fenves (1998); Lubliner et al. (1989), integrating distinct hardening/softening responses under tensile and compressive loading. Critical parameters governing the CDP formulation include the dilation angle (ψ), which controls volumetric expansion during plastic flow; the flow potential eccentricity (ϵ), adjusting the plastic potential surface shape; the biaxial/uniaxial compressive strength ratio (σ_{bo}/σ_{co}), defining multiaxial stress interactions; and the second stress invariant ratio (K_c), influencing deviatoric stress contributions. These parameters, calibrated for the 3D simplified micromodel and tabulated in Table 1 (Tariq et al., 2023). The uniaxial compressive stress-strain relationship is characterized by linear elasticity up to an ultimate strain of 0.003, followed by a plastic regime with hardening until peak stress at a strain of 0.005 (Abdulla et al., 2017). Post-peak behavior transitions to strain-softening, representing progressive micro-crack and crushing. The mechanical properties of the mortar joint interface between masonry units are outlined in Table 2 to Table 4 (Abdulla et al., 2017). The framework ensures close alignment with experimental observations of masonry behavior under complex loading, validating its predictive capability for structural failure mechanisms.

The boundary conditions replicate the experimental setup, where the model base is fully restrained at the bottom, and a vertical compressive stress of 0.3 MPa is applied to the top. Once the vertical load is applied, the top beam is restrained against vertical and out-of-plane displacements, and a quasi-static in-plane horizontal displacement of 4 mm is incrementally imposed via the top beam, restricting movement exclusively to the direction of the applied force. This simulation approach reflects the experimental configuration used to test masonry walls as reported in Lourenco (1996); Raijmakers and Vermeltfoort (1992),

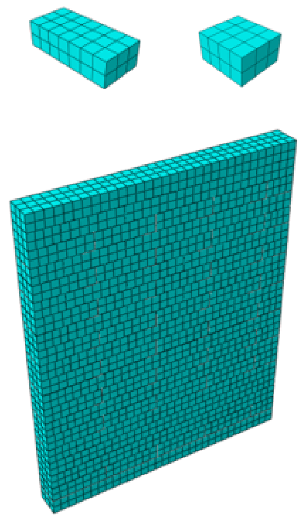

(a)

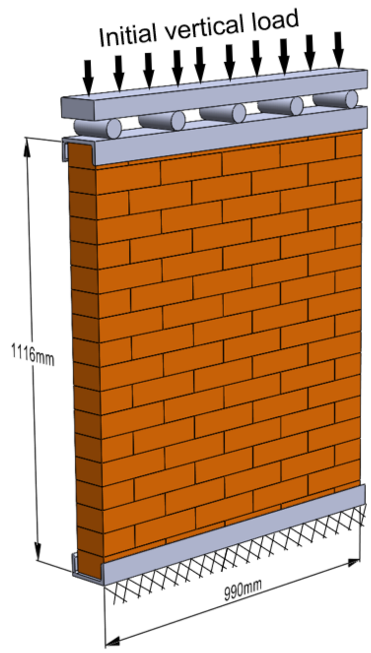

(b)

Figure 2: Masonry shear wall, (a) unit with different mesh size for full and half brick (top) and (b) test setup(Abdulla et al., 2017)

Table 1: Material properties for CDP model (adapted from Tariq et al. (2023))

Dilation angle (ψ)	Eccentricity (ϵ)	σ_{b0}/σ_{c0}	K_c
31	0.1	1.16	0.667

Table 2: Elastic properties of masonry unit, top steel beam, and joint interface for in-plane loading (adapted from Abdulla et al. (2017))

Brick units			Top steel beam			Mortar	Joint interface		
Density (kg/m^3)	E_u (MPa)	ν	Density (kg/m^3)	E_{beam} (MPa)	ν	E_m	K_n (N/mm^3)	K_s (N/mm^3)	K_t (N/mm^3)
2000	16700	0.15	7830	207000	0.30	780	82	36	36

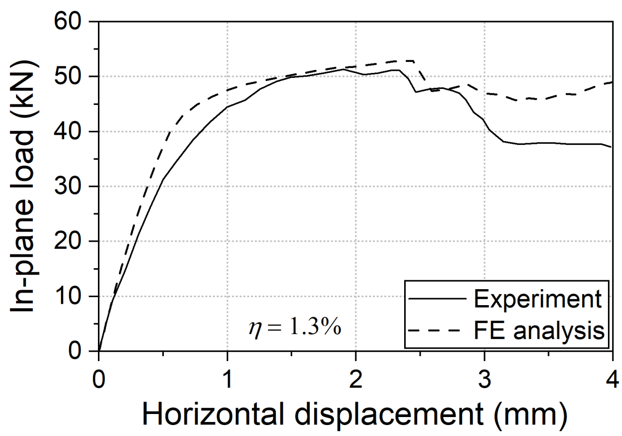

Figure 3: Pushover curve comparison between experiment and FE analysis

where typical failure modes included diagonal cracking, unit rupture, and compressive crushing.

The numerical model is rigorously validated against experimental benchmarks from Lourenço and Rots (1997), as shown in Figure 3. The modeling approach was guided by previous successful implementations, particularly Abdulla et al. (2017). Key validation metrics include the pushover curve alignment, failure mode consistency, and stress redistribution mechanism. The simulated load-displacement relationship exhibits a strong correlation with experimental results, achieving a root mean square error (RMSE) of 1.3%, Figure 3. The peak lateral strength of the numerical model (52.8 kN) deviates by only 1.2% from the experimental model (51.6 kN), underscoring capturing the accuracy of model in ultimate load capacity.

The qualitative agreement between the experimental and numerical crack patterns is demonstrated in Figure 4. The model successfully captures the key failure mechanism observed in the test. Specifically, both the experiment and numerical simulation shows the subsequent development of diagonal shear cracks propagation from supports towards the loading point. The final failure mode characterized by a critical shear crack causing loss of capacity. While the simulation shows a slightly more diffuse cracking pattern, the primary crack path and the overall failure mechanism are accurately reproduced, providing strong qualitative validation of the model's ability to simulate complex fracture behavior.

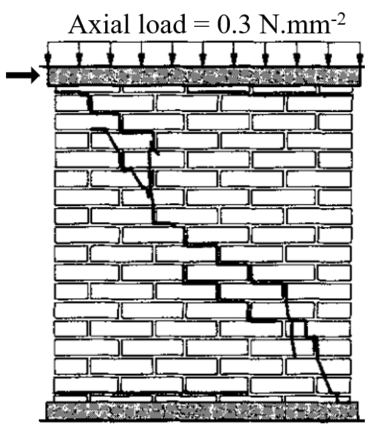

(a)

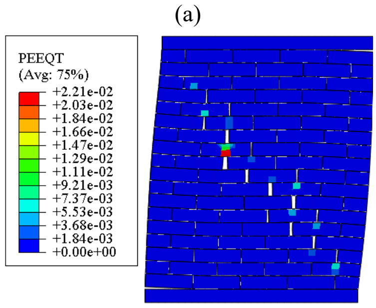

(b)

Figure 4: Comparision of damage pattern, (a) experimental damage pattern (Lourenço and Rots, 1997), (b) damage pattern in numerical model (scale factor = 20)

Figure 5a illustrates material degradation in the masonry unit, quantified by the compressive damage variable

Table 3: Tensile and shear properties for masonry unit (adapted from Abdulla et al. (2017))

Tension		Shear	
Tensile strength (MPa)	G_{IC} (N/mm)	Shear strength (MPa)	G_{IIC} (N/mm)
2.00	0.08	2.80	0.50

Table 4: Plastic properties for the joint interface (adapted from Abdulla et al. (2017) for Equations 10 to 12)

Tension		Shear			Compression, σ_c
$t_{n,\max}$ (MPa)	G_{IC} (N/mm)	Cohesion, c (MPa)	μ	G_{IIC} (N/mm)	(MPa)
0.25	0.02	0.35	0.75	0.13	10.50

(DAMAGEC). This parameter ranges from 0 (undamaged) to 1 (complete failure), with values between 0 and 0.02 indicating early-stage degradation where the unit retains nearly full stiffness. Such thresholds provide critical insights into stress/strain localization and guide design optimization. Furthermore, the stress transfer mechanism is analyzed via the minimum principal compressive stress (S, Min. Principal) in ABAQUS. Principal stresses represent normal stresses acting on planes with zero shear stress, where positive values denote compression and negative values signify tension. Figure 5b reveals the formation of a diagonal compressive strut under lateral loading, a key load-resisting mechanism. Simultaneously, tensile stress concentrations highlight vulnerable regions requiring reinforcement to mitigate premature failure. This dual stress-state visualization underscores the interaction between compressive load paths and tensile vulnerabilities in masonry systems.

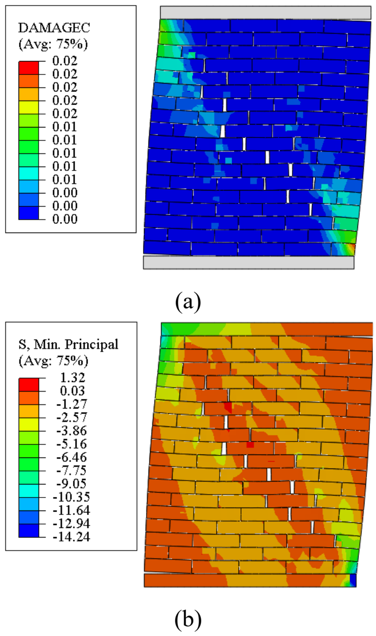

Figure 5: Response of wall at 4mm horizontal displacement, (a) compressive damage variable, (b) diagonal strut formation (scale factor = 20)

4. Parametric Analysis on Conventional Mortar Used in Nepal

Nepal suffered severe damage during the 2015 AD Gorkha earthquake. Buildings constructed with brick masonry using mud or lime-surkhi mortar experienced significant collapse due to the mortar's low binding capacity. Even heritage structures in Kathmandu, listed as UNESCO World Heritage Sites in 1979 AD, sustained major damage despite being considered robust prior to the earthquake (Bijukchhen et al., 2017). Following the disaster, these heritage buildings went through rigorous assessment and analysis to guide restoration efforts (Bahadur et al., 2021). Detailed studies were conducted on the mechanical properties of masonry units and mortars to improve seismic resilience. For instance, the mechanical behavior of mud mortar, widely used in traditional construction, has been evaluated through experimental testing (Endo and Miyoshi, 2023). Similarly, lime-surkhi-sand (1:1:3) mortar, a common material in heritage structures, has been analyzed to understand its structural performance (Parajuli, 2018).

Regarding unreinforced masonry, the Nepal National Building Code ("Guidelines for Earthquake Resistant Building Construction: Low Strength Masonry", 2015) recommends a cement-sand mortar mix ratio of 1:6. However, while "Guidelines for Earthquake Resistant Building Construction: Low Strength Masonry" (2015) specifies this ratio, it does not provide detailed mechanical properties for the 1:6 cement-sand mortar ("Guidelines for Earthquake Resistant Building Construction: Low Strength Masonry", 2015). To address this gap, the China National Code ("Code for Design of Masonry Structures", 2011) is referenced for supplementary material parameters ("Code for Design of Masonry Structures", 2011; Narayanan, 2013). A parametric analysis was conducted to systematically investigate the sensitivity of the structural response to mortar strength. This was achieved by modeling three distinct masonry types, defined exclusively through modifications to the mortar joint interfaces. The brick units and overall wall geometry were maintained consistent with the validated model presented in Section 3. The three mortar grades (representing low, medium, and high strength) were designed to encompass the characteristic range of materials commonly used in Nepal. The finalized sets of parameters defining each masonry type are detailed in Tables 5 and 6. While, the loading was performed in two main loading stages, where constant pre-compression vertical stress of 0.3 MPa was first applied, and then in-plane horizontal cyclic loads were applied under displacement control. Essentially, there were 21 cycles total placed on the wall, which is summarized in Figure 6 (“Standard Test Methods for Cyclic (Reversed) Load Test for Shear Resistance of Vertical Elements”, 2011).

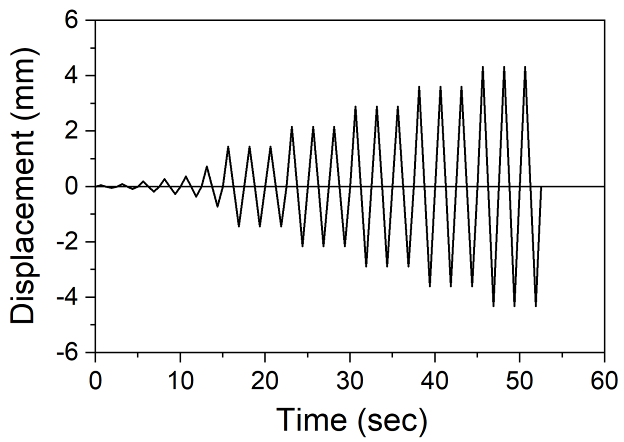

Figure 6: In-plane horizontal reversed cyclic loading

4.1. Response of Masonry Under In-plane Static and Cyclic Loading

The static in-plane load-displacement behavior reveals distinct differences among the mortar types, as shown in Figure 7a. Cement mortar exhibited the highest peak in-plane load, reaching 50 kN, with relatively ductile behavior, as evidenced by its sustained load capacity beyond the peak load. Lime-surkhi mortar achieved a moderate maximum load of approximately 30 kN but exhibited a sudden drop after reaching peak load, indicating brittle failure characteristics. In contrast, mud mortar displayed the lowest peak load (15 kN) and a gradual increase followed by abrupt load reduction, highlighting its inferior structural capacity and brittle behavior under static conditions. The cyclic loading response of cement mortar is illustrated in Figure 7b. Cement mortar displayed consistent hysteresis loops in the first several cycles of load, showing little degradation to the stiffness. The cement mortar also performed consistently over several cycles of load. The loops showed roughly symmetric loop shapes to varying magnitude and less degradation compared to lime-surkhi mortar shown in Figure 7c. The loops did suggest a slightly larger energy dissipation potential suggesting more favorable ductile behaviors. The lime-surkhi mortar exhibited moderate performance. Its hysteresis loops showed noticeable pinching and asymmetry, reflecting a moderate level of ductility and energy dissipation, along with more pronounced stiffness and strength degradation in the initial cycles compared to cement mortar. In contrast to the other mortars, the mud mortar demonstrated a classic brittle failure mechanism. Its hysteresis loop (Figure 7d) exhibits an initially linear elastic response until its peak, followed by abrupt softening. The subsequent degraded and narrow loops show a complete absence of pinching; a key indicator that the material lacks the inelastic, friction-based energy dissipation mechanisms that produced the stable, symmetric loops in cement mortar and the moderately pinched loops in lime-surkhi mortar. This confirms its very limited performance and unsuitability for cyclic loading.

4.2. Stiffness Degradation Analysis

Stiffness degradation refers to the progressive reduction in stiffness over successive loading cycles, a phenomenon that becomes evident as larger displacements occur under the same or reduced load magnitudes in later cycles. This behavior serves as a direct indicator of accumulating internal damage within the masonry, including micro-cracking, bond deterioration, and material softening. The extent of degradation provides critical insights into the structural integrity and residual capacity of the masonry under repeated loading conditions. For practical engineering analysis, the effective stiffness (K_{eff}) of a masonry wall is commonly adopted as a key parameter. This effective stiffness is typically quantified as the secant stiffness, derived from the envelope of the hysteresis curve, and is defined as the ratio of the peak lateral force to the corresponding peak displacement observed during cyclic testing of wall specimens or numerical models Sathiparan et al., 2012. Mathematically it is expressed in Equation (13),

$$K_i = \frac{|+F_i| + |-F_i|}{|+X_i| + |-X_i|} \tag{13}$$

where $+F_i$ and $-F_i$ are the peak loads, and $+X_i$ and $-X_i$ are the peak displacement in the positive (push) and negative (pull) loading direction, respectively Zhou et al., 2020.

The initial secant stiffness of cement, lime-surkhi, and mud mortars, under cyclic loading, was observed as a function of the secant stiffness of the hysteresis envelopes, as shown in Figure 8. Cement mortar begins with the highest secant stiffness (approximately 170 kN/mm), which drops

Table 5: Elastic properties of mortar used in Nepal

Mortar type	Elasticity	Joint interface			Source
	E_m	K_n (N/mm^3)	K_s (N/mm^3)	K_t (N/mm^3)	
Mud	–	3	1	1	Endo and Miyoshi (2023)
Lime-surkhi	142	14.32	5.73	5.73	Parajuli (2018)
Cement-sand	2000	227	91	91	"Code for Design of Masonry Structures" (2011)

Table 6: Tensile and shear properties for mortar used in Nepal

Mortar type	Tension		Cohesion, c	Shear		Compression, σ_c
	$t_{n,\max}$ (MPa)	G_{IC} (N/mm)	(MPa)	μ	G_{IIC} (N/mm)	(MPa)
Mud	0.02	0.003	0.014	0.30	0.030	1.70
Lime-surkhi	0.17	0.005	0.128	0.45	0.050	1.70
Cement-sand	0.24	0.007	–	0.75	0.050	6.7

sharply to around 40 kN/mm within 1 mm deformation. The early drop in stiffness indicates a change from almost entirely elastic behavior to primarily plastic, with much of the damage occurring early on. After the 1 mm deformation, the rate of stiffness decline is gradual and linear down to approximately 7 kN/mm, but indicates little residual stiffness at larger displacements.

Lime-surkhi mortar began with an initial secant stiffness of about 25 kN/mm and dropped slowly and steadily to about 5 kN/mm over the 0 – 4 mm displacement range. The gradual decrease in stiffness accords with the ductile behavior of lime-surkhi mortar, which represents the gradual micro-cracking and softening of the matrix due to the flexibility from the carbonation process.

For mud mortar, the secant stiffness was nearly constant at around 5 kN/mm through the initial displacement range of 3 mm. The constant stiffness slope, and the corresponding linear hysteretic behavior, indicates minimal stiffness degradation under low cyclic strain. Upon reaching a critical threshold, a sharp drop in stiffness occurred, and subsequent cyclic loops formed without pinching, resembling a friction-dominated sliding mechanism along a failed interface, which would indicate a shift from cohesive to residual frictional resistance.

Comparative analysis indicates that cement mortar exhibits by far the largest initial stiffness drop, which is approximately 75% within 1 mm displacement, which demonstrates that damage occurs quickly in the early stages. Lime-surkhi mortar has a significant loss of stiffness, about 80%, although the process is much smoother. Mud mortar, despite its low stiffness and relatively constant behavior, offers a somewhat more persistently stable cyclic response than expected, treating its lower strength and brittle/ low-strength capacity.

4.3. Mechanical Behaviour Under Cyclic Loading

Evaluating the cyclic loading behavior, based on the ABAQUS parameters PEEQT (equivalent plastic strain) and DAMAGET (tensile damage), provides further information regarding the mortar performance. The larger PEEQT values from the cement mortar are in line with a very quick transition from elastic to plastic behavior which means significant capacity for plastic deformation and ductility under cyclic loading. Figure 9a shows that the cement mortar sustained plastic strains across large areas from moderate to high levels especially in central locations and heavily loaded areas, emphasizing plastic deformation once again. The lime-surkhi mortar PEEQT levels are moderate, but it appears to show ductile behavior with the incremental amounts of point like plastic deformation being predominantly located around the peripheral areas of the brick and path of crack, Figure 9b, which means that the mortar experienced progressive and controlled plastic deformation from limited micro-cracking. The mud mortar on the other hand displayed minimal PEEQT resistance none to very little being positioned to the corners of the brick itself Figure 9c, suggesting an almost total absence of plastic deformation and followed by crack formation at joint.

DAMAGET analysis visually illustrates the extent of tensile damage across mortar types. In the case of cement mortar, there is extensive tensile damage across the central region, albeit confined mostly to the central region because of high initial damage susceptibility and dramatic decreases in mortar stiffness (Figure 9d). In the case of lime-surkhi mortar, a moderate amount of tensile damage was located in the outer edges (Figure 9e), which was consistent with the weaker mortars with slowly decreasing stiffness and slow damage progression. Finally, with respect to mud mortar, tensile damage was essentially non-existent except for a few small areas at the corners (Figure 9f), and this suggested the material was subjected to minimal tensile strain during the cyclic loading scenario, which was consistent to the stable

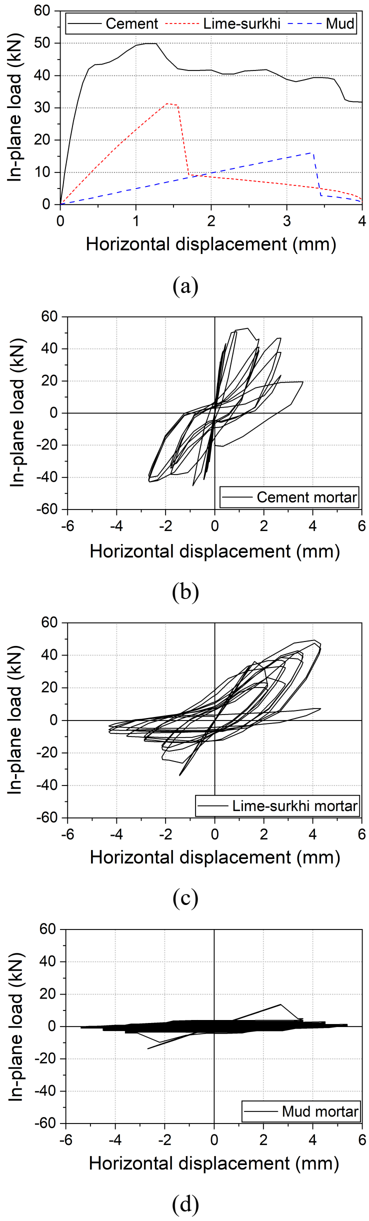

Figure 7: Linear and cyclic hysteresis response of masonry wall with different mortar type, (a) linear response of masonry wall, (b) wall with cement mortar, (c) wall with lime-surkhi mortar, (d) wall with mud mortar

trend of stiffness. Collectively, the interpretation of the PEEQT and DAMAGET analyses highlighted the important relationship of plastic deformation and tensile damage type behavior and also allowed us to better understand the performance of different mortars under cyclic loading conditions.

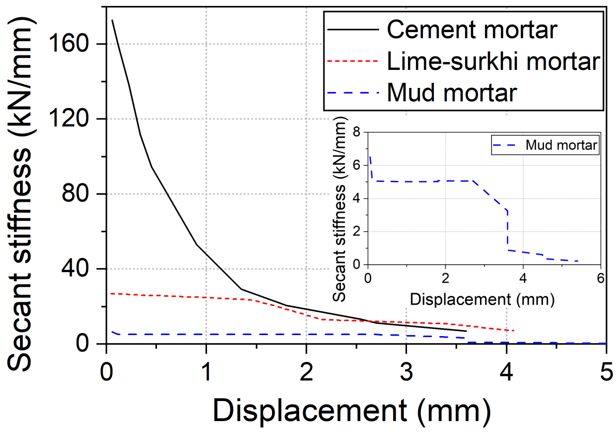

Figure 8: Secant stiffness degradation of cement, lime-surkhi, and mud mortar under cyclic loading

5. Conclusion

This research examined the cyclic in-plane response of masonry walls built with cement, lime-surkhi, and mud mortars, using a validated finite element model based on the simplified micro-modeling procedure in ABAQUS. The mechanical deterioration of the wall systems was evaluated using hysteresis-based secant stiffness, equivalent plastic strain (PEEQT), and tensile damage (DAMAGET). The main findings are summarized as follows:

- The model demonstrated strong agreement with experimental results. The validation showed an excellent match in the global load-displacement response, with an RMSE of 1.3%, and accurately captured the critical diagonal cracking failure mode, as confirmed by both quantitative metrics and direct visual comparison (see Figs. 4)

- The hysteretic response varied significantly among mortar types. Cement mortar produced wide, stable loops, indicating high energy dissipation and ductility. Lime-surkhi mortar exhibited moderately pinched loops, reflecting progressive stiffness degradation and moderate ductility. In contrast, mud mortar generated narrow loops, demonstrating minimal energy dissipation and classic brittle failure.

- The stiffness degradation patterns were distinct for each mortar type. Cement mortar underwent rapid softening, with its secant stiffness dropping approximately 75%—from (170 kN/mm to 43 kN/mm) within the first 1 mm of displacement, indicating swift yielding and post-elastic behavior. Lime-surkhi mortar exhibited a gradual, ductile reduction from 25 kN/mm to 5 kN/mm over 4 mm of displacement. In contrast, mud mortar maintained

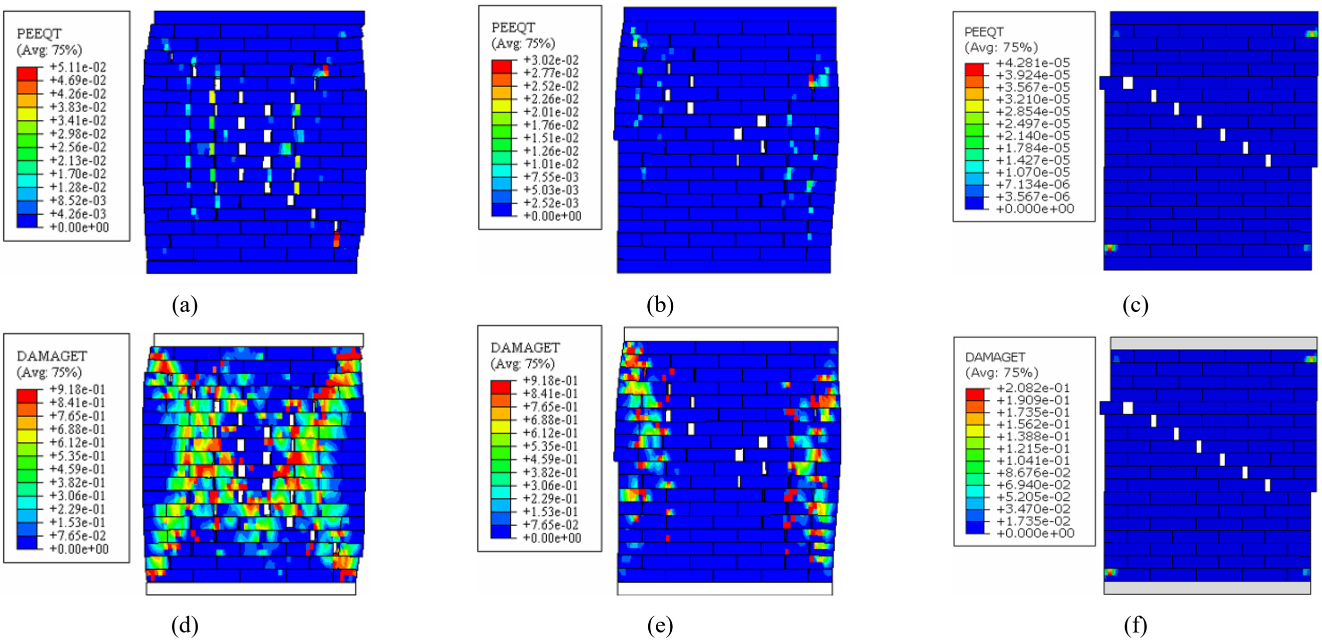

Figure 9: Distribution of equivalent plastic strain (PEEQT) and tensile damage (DAMAGET) in masonry wall with different mortar types, (a) and (d) wall with cement mortar, (b) and (e) wall with lime-surkhi mortar, (c) and (f) wall with mud mortar, (scale factor = 10)

a low, nearly constant stiffness (5 kN/mm) until its failure displacement of 3 mm, after which its load-bearing capacity dropped to a negligible level. This pattern signifies minimal usable strength and an absence of progressive damage accumulation, which is consistent with a brittle material response.

- The distribution of equivalent plastic strain (PEEQT) and tensile damage (DAMAGET) revealed the underlying failure mechanisms. Cement mortar sustained substantial plastic deformation (high PEEQT) with tensile damage concentrated centrally, indicating ductile, energy-dissipating failure. Lime-surkhi mortar developed moderate plastic strain with damage localized at the perimeter, consistent with controlled cracking. Mud mortar showed negligible levels of both PEEQT and DAMAGET, confirming a lack of inelastic deformation and brittle, strength-limited failure.

Based on the comparative analysis of hysteretic response, stiffness degradation, and damage evolution, lime-surkhi mortar emerges as the most favorable option for masonry under moderate cyclic stresses due to its balanced combination of strength and controlled, progressive damage. While cement mortar provides high initial stiffness and energy dissipation, its rapid loss of stiffness under high loads necessitates careful design and potential reinforcement in severe seismic applications. Conversely, the brittle failure, negligible energy dissipation, and minimal damage tolerance demonstrated by mud mortar restrict its use to non-structural applications only.

References

Abdulla, K. F., Cunningham, L. S., & Gillie, M. (2017). Simulating masonry wall behaviour using a simplified micro-model approach. *Engineering Structures*, *151*, 349–365. https://doi.org/10.1016/j.engstruct.2017.08.021

Alcaino, P., & Santa-Maria, H. (2008). Experimental response of externally retrofitted masonry walls subjected to shear loading. *Journal of Composites for Construction*, *12*(5), 489–498. https://doi.org/10.1061/(ASCE)1090-0268(2008)12:5(489)

Bahadur, G., Kumar, B., & Jha, P. (2021). Structural condition assessment and retro fitting of shital niwas building (presidential palace). *Progress in Disaster Science*, *10*, 100174. https://doi.org/10.1016/j.pdisas.2021.100174

Benzeggagh, M. L., & Kenane, M. (1996). Measurement of mixed-mode delamination fracture toughness of unidirectional glass/epoxy composites. *Composites Science and Technology*, *56*, 439–449.

Bijukchhen, S., Takai, N., Shigefuji, M., Ichiyanagi, M., & Sasatani, T. (2017). Strong-motion characteristics and visual damage assessment around seismic stations in kathmandu after the 2015 gorkha earthquake. *Earthquake Spectra*, *33*, 219–242. https://doi.org/10.1193/042916EQS074M

Building code requirements and specification for masonry structures. (2013). ACI.

Code for design of concrete structures. (2010). China Standards.

Code for design of masonry structures. (2011). China Standards.

Degryse, P., Elsen, J., & Waelkens, M. (2002). Study of ancient mortars from sagalassos (turkey) in view of their conservation. *Cement and Concrete Research*, *32*(9), 1457–1463. https://doi.org/10.1016/S0008-8846(02)00807-4

Design of masonry structures - part 1-1. (2005). CEN.

Endo, Y., & Miyoshi, K. (2023). Meso-scale numerical simulation of the mechanical behaviour of brick masonry in earth mortar. *Journal of Building Engineering*, *74*, 106890. https://doi.org/10.1016/j.jobe.2023.106890

Fang, S. Q., Zhang, H., Zhang, B. J., & Zheng, Y. (2014). The identification of organic additives in traditional lime mortar. *Journal of Cultural Heritage*, *15*(2), 144–150. https://doi.org/10.1016/j.culher.2013.04.001

Guidelines for earthquake resistant building construction: Low strength masonry. (2015). NBC Nepal.

Jafari, S., Rots, J. G., Esposito, R., & Messali, F. (2017). Characterizing the material properties of dutch unreinforced masonry. *Procedia Engineering*, *193*, 250–257. https://doi.org/10.1016/j.proeng.2017.06.211

Khattak, N., Derakhshan, H., Thambiratnam, D. P., Malomo, D., & Perera, N. J. (2023). Modelling the in-plane/out-of-plane interaction of brick and stone masonry structures. *Journal of Building Engineering*, *76*, 107175. https://doi.org/10.1016/j.jobe.2023.107175

Knox, C. L., Dizhur, D., & Ingham, J. M. (2018). Experimental study on scale effects in clay brick masonry. *Construction and Building Materials*, *163*, 706–713. https://doi.org/10.1016/j.conbuildmat.2017.12.149

Lee, J., & Fenves, G. L. (1998). Plastic-damage model for cyclic loading of concrete structures. *Journal of Engineering Mechanics*, *124*(8), 892–900.

Liang, B., Zhang, H., Liu, Z., & Hou, J. (2023). The influence of different types of mortar on the compressive strength of masonry. *Journal of Building Engineering*, *65*, 105635. https://doi.org/10.1016/j.jobe.2022.105635

Lotif, R., & Shing, P. B. (1994). Interface model applied to fracture of masonry structures. *Journal of Structural Engineering*, *120*(1), 63–80.

Lourenco, P. B. (1996). *Computational strategies for masonry structures* [Doctoral dissertation, Delft University of Technology].

Lourenço, P. B., & Rots, J. G. (1997). Multisurface interface model for analysis of masonry structures. *Journal of Engineering Mechanics*, *123*(7), 660–668. https://doi.org/10.1061/(ASCE)0733-9399(1997)123:7(660)

Lubliner, J., Oliver, J., Oller, S., & Oñate, E. (1989). A plastic-damage model for concrete. *International Journal of Solids and Structures*, *25*(3), 299–326. https://doi.org/10.1016/0020-7683(89)90050-4

Minafò, G., & La Mendola, L. (2018). Effect of mortar grade on the compressive behaviour of frcm confined masonry columns. *Composites Part B*, *146*, 1–12. https://doi.org/10.1016/j.compositesb.2018.03.033

Narayanan, S. P. (2013). Properties of brick masonry for fe modeling. *American Journal of Engineering Research*, 1–6.

Parajuli, H. R. (2018). Mechanical properties for surkhi bonded kathmandu world heritage buildings. *Asian Journal of Science and Technology*, *9*(8), 8467–8472.

Raijmakers, T. M., & Vermeltfoort, A. T. (1992). *Deformation controlled tests in masonry shear walls*.

Ravula, M. B., & Subramaniam, K. V. L. (2017). Experimental investigation of compressive failure in masonry brick assemblages. *Materials and Structures*, *50*(1), 1–11. https://doi.org/10.1617/s11527-016-0926-1

Sathiparan, N., Mayorca, P., & Meguro, K. (2012). Shake table tests on masonry houses retrofitted with pp-band mesh. *Earthquake Spectra*, *28*(1), 277–299. https://doi.org/10.1193/1.3675357

Senthivel, R., & Lourenço, P. B. (2009). Finite element modelling of historical stone masonry shear walls. *Engineering Structures*, *31*(9), 1930–1943. https://doi.org/10.1016/j.engstruct.2009.02.046

Singh, S. B., & Munjal, P. (2017). Bond strength and compressive stress-strain characteristics of brick masonry. *Journal of Building Engineering*, *9*, 10–16. https://doi.org/10.1016/j.jobe.2016.11.006

Standard test methods for cyclic (reversed) load test for shear resistance of vertical elements. (2011). ASTM.

Tariq, H., Najafgholipour, M. A., Sarhosis, V., & Milani, G. (2023). In-plane strength of masonry wall panels.

Structures, *47*, 1869–1899. https://doi.org/10.1016/j.istruc.2022.11.125
Xia, Y., Li, X., Zhu, R., Yi, G., & Li, J. (2023). Experimental investigation and numerical simulation of masonry walls. *Structures*, *56*, 105025. https://doi.org/10.1016/j.istruc.2023.105025
Yuen, T. Y. P., Deb, T., Zhang, H., & Liu, Y. (2019). A fracture energy based damage-plasticity interfacial constitutive law. *Computers and Structures*, *220*, 92–113. https://doi.org/10.1016/j.compstruc.2019.05.007
Zhang, S., Yang, D., Sheng, Y., Garrity, S. W., & Xu, L. (2017). Numerical modelling of frp-reinforced masonry walls. *Construction and Building Materials*, *134*, 649–663. https://doi.org/10.1016/j.conbuildmat.2016.12.091
Zhou, Q., Yang, L., & Zhao, W. (2020). Experimental analysis of seismic performance of masonry shear wall reinforced with pp-band mesh. *Advances in Civil Engineering*, *2020*. https://doi.org/10.1155/2020/4015790

This page is intentionally left blank.